Trapped structures in drift wave turbulence

Cite as: Physics of Fluids B: Plasma Physics **4**, 2854 (1992); https://doi.org/10.1063/1.860160
Submitted: 16 April 1991 . Accepted: 14 April 1992 . Published Online: 01 September 1998

James A. Crotinger and Thomas H. Dupree

Trapped structures in drift wave turbulence

James A. Crotinger
Lawrence Livermore National Laboratory, P.O. Box 808, L-630, Livermore, California 94550

Thomas H. Dupree
Massachusetts Institute of Technology, Cambridge, Massachusetts 02139

(Received 16 April 1991; accepted 14 April 1992)

The development of trapped structures in decaying and saturated drift wave turbulence is studied via computer simulation. A two-dimensional electrostatic fluid model is used. The turbulence that evolves in the pure decay runs (i.e., no nonadiabatic electrons) is characterized by tightly bound monopole vortices and a very narrow frequency spectrum. For the studies of saturated turbulence, a new nonadiabatic electron model is introduced, which gives the qualitatively correct response to a coherent trapped structure. This model takes into account the effects of broadening and shifting of the frequency spectrum. These effects are found to be quite important. Trapped structures are observed in many of the saturated simulations, even in the presence of moderately broad frequency spectra. The extent of the trapping varies dramatically, becoming a much stronger effect as the average electric field increases.

I. INTRODUCTION

In this paper we examine the role of coherent "trapped" structures in drift wave turbulence via the direct numerical simulation of two-dimensional model equations. Several other authors[1-8] have studied two-dimensional drift wave turbulence using equations similar to those studied here. Our work has a somewhat different focus, however, in its concentration on trapped structures in fully developed turbulence. Furthermore, we introduce a new model for the nonadiabatic electron response—one that gives the qualitatively correct response of the electrons to a coherent structure. We study the effects of this new model in some detail.

What, exactly, do we mean by "trapped structure?" If an isolated potential fluctuation is sufficiently large and long lived, the resulting electric field will trap elements (or "particles") of fluid, causing them to move in a coherent fashion along with the fluctuation. For this trapping to occur, two conditions must be satisfied: First, the electric field must be sufficiently large to overcome the natural tendency for the fluctuation to move away from the particle at the diamagnetic drift speed. Second, the fluctuation must be coherent, with a long lifetime compared with the diamagnetic drift time scale.

We are concerned with the presence of trapped structures because their existence, and, in particular, their long lifetime, seems to contradict assumptions of popular turbulence theories. Weak turbulence theory,[9] resonance broadening theory,[10] and the direct interaction approximation (DIA)[11] make assumptions about the modes having "random phases" or being "maximally random." However, the evolution of the particles within a trapped structure is completely nonchaotic during the structure's lifetime. Furthermore, these randomness assumptions remove all information about phase correlations from the theories. These phase correlations contain the information describing the evolution and interaction of trapped structures. Although one can argue that the ensemble average loses the phase information but retains the appropriate statistical information arising from the structure evolution, this is not *a priori* clear. Indeed, closure theories are perturbative in nature, whereas coherent structures are inherently nonperturbative. Dupree's clump theory[12] does take into account the correlated motion of nearby particles. However, it too is perturbative and cannot account for the correlation of particles that are widely separated but that lie within the same trapped structure.

The equations studied in this paper, and in the references above, are extensions of the Hasegawa–Mima equation. Hasegawa and Mima introduced this equation in Ref. 1. Their initial work was theoretical, predicting the potential spectrum for two cases: the undriven, undamped case, which is amenable to an equilibrium statistical mechanics treatment; and the case where the turbulence is driven at large scales and damped at small scales. Fyfe and Montgomery[3] performed simulations of the Hasegawa–Mima equation for both of these cases (though they neglected the mean density gradient). They verified the predictions of equilibrium statistical mechanics. However, they found that spectrum for the driven-damped simulation was much steeper than that predicted by Hasegawa and Mima. We note that their simulations were at a rather low resolution. Waltz[4] introduced an *ad hoc* nonadiabatic electron response designed to reproduce features of the drift wave instability. This addition also introduced a new nonlinearity, due to the $\mathbf{E}\times\mathbf{B}$ convection of the nonadiabatic density. He made an interesting comparison of his simulation results with predictions of a closure code. Unfortunately, his work was also done at a relatively low resolution. Terry and Horton performed similar simulations, but with a slightly different nonadiabatic electron model. Their papers[5,6] dealt with very low resolution approximations (3 modes and 20 modes). In Horton's 1986 paper,[7] the same model was simulated at a more reasonable resolution of 128×128 modes. In this paper he concen-

 0899-8213/92/092854-17$04.00

trated on the statistical properties of the Fourier modes. However, decaying turbulence was also studied using the Hasegawa–Mima equation with viscous damping, and it was noted that long-lived structures formed in the potential. Such structures were not observed in the driven-damped case. In his recent paper,[8] he made a detailed study of the evolution and interaction of isolated monopole and dipole vortices, and made some theoretical predictions of how vortex collisions would enhance transport.

In this paper we show that trapped structures can form in strongly driven drift wave turbulence. Furthermore, our interest in trapped structures led us to reexamine the nonadiabatic electron models that were used in previous work. These models were found to give an incorrect response to coherent structures (at least for the electron drift wave) due to the fact that they fail to account for shifting and broadening of the frequency spectrum. A new model was implemented that gives the qualitatively correct response.

Section II of this paper presents the model equations and some of their properties. While these equations neglect a great deal of important physics (gyrokinetic effects, kinetic electron effects, magnetic shear, etc.), they maintain the main nonlinearity in the problem and are sufficiently simple that we can afford to solve them many times with a fairly high resolution. In Sec. III we briefly discuss the code used to solve these equations. Section IV contains a study of the evolution of decaying turbulence by solving the Hasegawa–Mima equation. In this case we find that the system naturally evolves to a quasisteady state characterized by many large coherent monopole vortices and a narrow frequency spectrum. Section V contains results from simulations of the new model equation. These solutions exhibit a much broader frequency spectrum, and the behavior of trapped structures—when they develop—is seen to be much more erratic. We study the role of the new nonadiabatic electron response in saturating the turbulence. Our results are summarized and discussed in Sec. VI.

II. MODELS

A. The Hasegawa–Mima equation

First we shall review the Hasegawa–Mima equation[1,2] and some of its properties. In nondimensional variables this equation may be written as

$$\left(\frac{\partial}{\partial t}+\mathbf{v}_E\cdot\nabla_\perp\right)(\phi-\nabla_\perp^2\phi)+v_d(x)\frac{\partial\phi}{\partial y}+\nu\nabla_\perp^4\phi=0, \tag{1}$$

where ϕ is the electrostatic potential, $\mathbf{v}_E\equiv\hat{\mathbf{z}}\times\nabla_\perp\phi$ is the $\mathbf{E}\times\mathbf{B}$ drift velocity, v_d is the diamagnetic drift velocity, and ν is an *ad hoc* viscosity. The x coordinate represents the radial direction and the y coordinate, the poloidal direction. The nondimensional variables are motivated by the length and time scales for electron drift waves:

$$x=\frac{x'}{\rho_s},\quad y=\frac{y'}{\rho_s},\quad z=\frac{z'}{L_n},\quad t=\frac{c_s}{L_n}t', \tag{2}$$

where the primed quantities are the dimensional variables, ρ_s is the ion gyroradius at the electron temperature, L_n is the scale length of the equilibrium density gradient, and c_s is the ion sound speed. The dimensionless electrostatic potential is defined as

$$\phi=\frac{L_n}{\rho_s}\frac{e\phi'}{T_e}. \tag{3}$$

This definition is based on the observation that drift waves saturate at an amplitude

$$\frac{e\phi'}{T_e}\sim\frac{\rho_s}{L_n},$$

so we have scaled the dimensionless potential, such that $\phi\sim 1$.

Throughout this paper we shall take the equilibrium density to be an exponential with constant scale length L_n, in which case $v_d=1$ (due to our scaling for the potential) and Eq. (1) becomes homogeneous in x. This allows us to solve Eq. (1) on a periodic domain, where the potential may be expanded in a Fourier series in both x and y as follows:

$$\phi(x,y,t)=\sum_{k_x,k_y}\phi_{\mathbf{k}}(t)e^{ik_x x+ik_y y}.$$

In the inviscid limit, Eq. (1) possesses important conservation properties. First there is a local conservation property made explicit by writing the equation in convection form:

$$\left(\frac{\partial}{\partial t}+\mathbf{v}_E\cdot\nabla_\perp\right)\rho=\nu\nabla_\perp^4\phi, \tag{4}$$

where

$$\rho\equiv x-\phi+\nabla_\perp^2\phi.$$

Thus, in the inviscid limit, ρ is conserved along the trajectory of a fluid element. This local conservation property gives rise to an infinite family of integral invariants that may be obtained by integrating any function of ρ over a domain whose boundary is a closed material line (i.e., moves with the fluid).

An important point to note is the explicit linear dependence of ρ on x. This dependence puts a severe constraint on the motion of a fluid element, since the distance that a fluid element can stray from its equilibrium (i.e., $\phi=0$) x position is limited by the total energy in the system. Thus, in the absence of viscosity, diffusion in the x direction is prohibited. Even in the presence of viscosity, diffusion is very anisotropic. In later sections we will see that the x dependence of ρ has several other implications.

The two-dimensional Navier–Stokes equations may also be written in the form of Eq. (4), but with $\rho=\nabla_\perp^2\phi$, the fluid vorticity (which is related to the local rotation rate of the fluid). For this reason, ρ is sometimes referred to as the potential vorticity.

Equation (1) also possesses several other integral invariants that are not obtainable from the conservation of ρ.[13] Of all the inviscid invariants, only two of these non-ρ invariants are conserved if the Fourier spectrum is trun-

cated to a finite number of modes. These are the energy E and the generalized enstrophy Ω, defined as

$$E=\int (\phi^2+\nabla_\perp\phi\cdot\nabla_\perp\phi)d^2x=\sum_{\mathbf{k}}(1+k^2)|\phi_{\mathbf{k}}|^2 \tag{5}$$

and

$$\Omega=\int [(\nabla_\perp^2\phi)^2+\nabla_\perp\phi\cdot\nabla_\perp\phi]d^2x=\sum_{\mathbf{k}}k^2(1+k^2)|\phi_{\mathbf{k}}|^2. \tag{6}$$

If viscosity is nonzero it is easy to show that the energy and enstrophy integrals obey

$$\frac{dE}{dt}=-2\sum_{\mathbf{k}}\nu_k(1+k^2)|\phi_{\mathbf{k}}|^2 \tag{7}$$

and

$$\frac{d\Omega}{dt}=-2\sum_{\mathbf{k}}\nu_k k^2(1+k^2)|\phi_{\mathbf{k}}|^2, \tag{8}$$

where $\nu_k=\nu k^4$ for normal fluid viscosity. (In our simulations we often use a "hyperviscosity," $\nu_k=\nu_4 k^6$, which effectively increases the viscous Reynolds number for the problem without requiring a larger grid.[14])

The existence of these two invariants, along with the conservative nature of the inviscid equations, allow equilibrium statistical mechanics to be used to predict average properties of the inviscid system.[2,3,15] The equilibrium statistical mechanics prediction for the potential spectrum is

$$\langle|\phi_{\mathbf{k}}|^2\rangle=\frac{1}{(1+k^2)(\alpha+\beta k^2)}, \tag{9}$$

and thus the isotropic energy and enstrophy spectra (defined such that $E=\Sigma_k E_k$, etc.) are

$$E_k=2\pi k(1+k^2)\langle|\phi_{\mathbf{k}}|^2\rangle=\frac{2\pi k}{\alpha+\beta k^2} \tag{10}$$

and

$$\Omega_k=k^2E_k=\frac{2\pi k^3}{\alpha+\beta k^2}. \tag{11}$$

Given E and Ω satisfying $k_{\min}^2 < k_*^2 < k_{\max}^2$, with $k_*^2\equiv\Omega/E$, these equations may be summed and inverted to obtain the constants α and β.[16] Furthermore, for moderate values of k_* the equilibrium energy spectrum, E_k, decreases at high-k and the equilibrium enstrophy spectrum increases. This tendency of the system to push energy to long scales and enstrophy to short scales is the driving force behind the well-known dual cascade.

Since the system tries to drive enstrophy to small scales, where viscous damping is strongest, the enstrophy will be strongly damped. Similarly, the energy is driven to long scales where the viscosity is very weak, and thus will only be weakly damped.

B. Nonadiabatic electrons

If the nonadiabatic electron density $\hat{n}$ is kept in the derivation of the Hasegawa–Mima equation, one obtains the following:

$$\left(\frac{\partial}{\partial t}+v_{E^*}\cdot\nabla_\perp\right)(\phi-\nabla_\perp^2\phi+\hat{n})+v_d(x)\frac{\partial\phi}{\partial y}+\nu\nabla_\perp^4\phi=0. \tag{12}$$

Note that this equation may still be written in the form of Eq. (4), but with $\rho\equiv x-\phi-\hat{n}+\nabla_\perp^2\phi$. Thus the inviscid equation still possesses many integral invariants. However, the important energy and enstrophy invariants are destroyed since, in the presence of the nonadiabatic electron density, there can be a nonvanishing net flux of energy and enstrophy into the domain.

To close the system we must calculate the nonadiabatic electron density in terms of the potential. This response may be found using the drift kinetic equation. For the collisionless electron drift wave in the low-frequency limit, $\omega\ll k_\parallel v_{Te}$, $\hat{n}$ is given approximately by

$$\hat{n}_{\mathbf{k}\omega}=i\delta_0(\omega-k_y)\phi_{\mathbf{k}\omega}, \tag{13}$$

where

$$\delta_0\equiv\frac{\sqrt{\pi}}{(k_\parallel L_n)(v_{Te}/c_s)}\sim\frac{\omega}{k_\parallel v_{Te}}, \tag{14}$$

$k_\parallel$ is the wavelength parallel to the magnetic field, v_{Te} is the electron thermal velocity, and c_s is the ion sound speed. This may be transformed back to the space-time domain to give

$$\hat{n}=-\delta_0\left(\frac{\partial}{\partial t}+\frac{\partial}{\partial y}\right)\phi. \tag{15}$$

One might consider solving Eqs. (12) and (15) as a coupled system for the density and potential. This approach will not work. The resulting second-order system has two eigenfrequencies. One corresponds to the oscillation of the potential vorticity, $\phi-\nabla_\perp^2\phi$, and gives the correct linear frequency and growth rate:

$$\omega_-=\frac{k_y}{1+k^2}+i\delta_0\frac{k_y^2k^2}{(1+k^2)^3}.$$

The other eigenfrequency corresponds to the relaxation of the density to near-adiabaticity. This occurs on a time scale much faster than the drift wave frequency. Equation (13) is not valid on this time scale. Indeed, the eigenfrequency predicted by the above system,

$$\omega_+=\frac{k_yk^2}{1+k^2}+i\delta_0^{-1}(1+k^2),$$

does not even have the correct sign for the imaginary part!

The problem with this approach is that Eq. (15) is not meant to be an evolution equation for the potential; rather, it gives the response *on the drift wave time scale* of the density to the potential fluctuations. The model equations we eventually solve should reflect this by being first order in time and using some approximation to Eq. (15) to close the system.

Previous work by Terry and Horton,[5,6] Horton,[7,8] Waltz,[4] and others, has made use of the so-called $i\delta$ approximation to avoid this difficulty. They assume that the linear frequency may be used for the purpose of calculating $\hat{n}$. This leads to

$$\hat{n}_{\mathbf{k}}(t)=i\delta_{\mathbf{k}}\phi_{\mathbf{k}}(t), \tag{16}$$

where

$$\delta_{\mathbf{k}}\equiv\delta_0(\omega_{\mathbf{k}}-k_y). \tag{17}$$

The $i\delta$ approximation gives the correct linear growth rate by design. Models using this approximation are the simplest model that lead to driven-damped steady states with transport, and have been studied a great deal. However, for the electron drift wave they do not give, even qualitatively, the correct response to a coherent structure. Suppose there is a coherent structure in the plasma traveling with a constant velocity in the poloidal direction:

$$\phi(x,y,t)=\phi(x,y-ct).$$

Substituting this into Eq. (13) gives

$$\hat{n}_{\mathbf{k}}=-i\delta_0(1-c)k_y\phi_{\mathbf{k}}. \tag{18}$$

If this is small, one may treat it as a perturbation in Eq. (12), leading to the following linear growth rate for the structure:

$$\gamma=\frac{\delta_0 c(1-c)k_y^2}{1+k^2}. \tag{19}$$

Thus, coherent structures with $c>1$ or $c<0$ (e.g., dipole modons[17]) will be damped by the nonadiabatic electrons. The $i\delta$ model misses this type of effect completely.

The $i\delta$ model also misses another type of effect: that of spectral broadening. Experimental measurements of turbulence in tokamaks show that the frequency spectrum of the potential fluctuations can be quite broad (as well as shifted away from $\omega_{\mathbf{k}}$).[18] Broad frequency spectra have also been observed in simulations of various models, including those that employ the $i\delta$ approximation.[7] However, it is clear that these effects are not included in Eq. (16).

The effects of frequency broadening and shifting may be described by a slow-time-scale energy equation. We write Eq. (12) in Poisson bracket form:

$$\frac{\partial\psi}{\partial t}+\{\phi,\psi\}+\frac{\partial\phi}{\partial y}=0, \tag{20}$$

where $\psi=x-\rho=\phi+\hat{n}-\nabla_\perp^2\phi$ and where $\{\cdot,\cdot\}$ is the Poisson bracket operator. Clearly the ϕ and ψ moments still annihilate the nonlinearity in Eq. (20). However, unless there is a simple relationship between ϕ and $\hat{n}$, this does not lead to a constant of the motion:

$$\frac{\partial}{\partial t}\frac{1}{2}\int\psi^2=-\int\psi v_{Ex}=-\int\hat{n}v_{Ex}. \tag{21}$$

There can now be a nonzero net influx of vorticity into our periodic domain. Similarly, the ϕ moment leads to the following equation:

$$\frac{\partial}{\partial t}\frac{1}{2}\int(\phi^2+\nabla_\perp\phi\cdot\nabla_\perp\phi)=-\int\phi\frac{\partial\hat{n}}{\partial t}. \tag{22}$$

To derive the slow-time-scale version of this equation we use Eq. (15) in Eq. (22), expand the time dependencies of the modes via a Fourier transform, and average over a period of time long compared to the drift wave period. The left-hand side is assumed to vary only on the slow time scale, which we denote by τ. This leads to the following slow time energy equation:

$$\frac{dE}{d\tau}=-\sum_{\mathbf{k}}(\nu_{\mathbf{k}}-\gamma_{\mathbf{k}}^{\mathrm{NL}})E_{\mathbf{k}}, \tag{23}$$

where γ_k^{NL} is a nonlinear growth rate defined by

$$\gamma_{\mathbf{k}}^{\mathrm{NL}}\equiv-\frac{\delta_{\mathbf{k}}}{E_{\mathbf{k}}}\sum_{\omega}\omega(\omega-k_y)|\phi_{\mathbf{k}\omega}|^2. \tag{24}$$

The frequency spectrum may be characterized by an average frequency, $\bar{\omega}$, and a frequency spread, $\Delta\omega$, defined by

$$\bar{\omega}_{\mathbf{k}}\equiv\frac{1}{|\phi_{\mathbf{k}}|^2}\sum_{\omega}\omega|\phi_{\mathbf{k}\omega}|^2 \tag{25}$$

and

$$\Delta\omega_{\mathbf{k}}^2\equiv\frac{1}{|\phi_{\mathbf{k}}|^2}\sum_{\omega}(\omega-\bar{\omega}_{\mathbf{k}})^2|\phi_{\mathbf{k}\omega}|^2. \tag{26}$$

In terms of these, the nonlinear growth rate may be written as

$$\gamma_{\mathbf{k}}^{\mathrm{NL}}=-\frac{\delta_{\mathbf{k}}}{1+k^2}[\Delta\omega_{\mathbf{k}}^2+\bar{\omega}_{\mathbf{k}}(\bar{\omega}_{\mathbf{k}}-k_y)]. \tag{27}$$

In the linear and weak turbulence regimes, $\bar{\omega}_{\mathbf{k}}\approx\omega_{\mathbf{k}}$ and $\Delta\omega_{\mathbf{k}}\approx0$; therefore $\gamma_{\mathbf{k}}^{\mathrm{NL}}$ reduces to the linear growth rate. The Terry–Horton description for the nonadiabatic electron response is appropriate in these regimes. If the turbulence is strong, however, both $\Delta\omega_{\mathbf{k}}$ and $\bar{\omega}_{\mathbf{k}}$ may change significantly from their linear values. Equation (27) shows how these changes will affect the energy balance: if the spectrum is broadened, or if the $\bar{\omega}_{\mathbf{k}}$ is shifted up past k_y, then the nonadiabatic electrons will become a sink of energy, rather than a source.

Note that these strong effects are somewhat peculiar to the collisionless drift wave. This instability is a very weak one. Other drift wave instabilities exist that possess a stronger drive, and that might, therefore, be less affected by the details of the frequency spectrum. However, the above analysis is still valid. The impact of changes in the frequency spectrum may not be as dramatic for these problems, but they may still be important. This is especially true when considering coherent structures, where $\bar{\omega}_{\mathbf{k}}$ may deviate significantly from the linear frequency.

Since we are interested in studying coherent structures as well as strong turbulence, we need a model that includes, at least qualitatively, these frequency spectrum effects. The $i\delta$ approximation is essentially a perturbation theory on the linear part of the equation. Our new model carries this idea one step further. First rewrite Eq. (12) as

$$\left(\frac{\partial}{\partial t}+\hat{\mathbf{z}}\times\nabla_\perp\phi\cdot\nabla_\perp\right)(\phi-\nabla_\perp^2\phi)+v_d(x)\frac{\partial\phi}{\partial y}+\nu\nabla_\perp^4\phi$$

$$=\delta_0\left(\frac{\partial}{\partial t}+\hat{\mathbf{z}}\times\nabla_\perp\phi\cdot\nabla_\perp\right)\left(\frac{\partial}{\partial t}+\frac{\partial}{\partial y}\right)\phi. \tag{28}$$

We assume that the right-hand side of Eq. (28) is small compared to the left-hand side, which is recognized as the Hasegawa–Mima equation.

The procedure is to approximate the $\partial/\partial t$ operators on the right-hand side of Eq. (28) using the Hasegawa–Mima equation. This should be correct to order $\hat{n}/\phi\sim\delta_0$. To this end we define

$$\dot{\phi}_0\equiv\left.\frac{\partial\phi}{\partial t}\right|_{\delta_0=0}=-P^{-1}\frac{\partial\phi}{\partial y}-P^{-1}\{\phi,P\phi\}, \tag{29}$$

where $P=1-\nabla_\perp^2$. Using Eq. (29) to approximate all time derivatives on the right-hand side of Eq. (28), we arrive at the following equation:

$$\left(\frac{\partial}{\partial t}+\hat{\mathbf{z}}\times\nabla_\perp\phi\cdot\nabla_\perp\right)(\phi-\nabla_\perp^2\phi)+v_d(x)\frac{\partial\phi}{\partial y}$$

$$=-\delta_0\left[P^{-1}(1-P^{-1})\frac{\partial^2\phi}{\partial y^2}+P^{-1}(1-P^{-1})\frac{\partial}{\partial y}\{\phi,P\phi\}\right.$$

$$\left.+P^{-1}\{\dot{\phi}_0,P\phi\}+P^{-1}\{\phi,P\dot{\phi}_0\}-\left\{\phi,\dot{\phi}_0+\frac{\partial\phi}{\partial y}\right\}\right]. \tag{30}$$

The right-hand side of Eq. (30) is only a function of ϕ and spatial operators on ϕ. The first term is the usual linear growth term.

Note that there is an alternative derivation, accurate to the same order in δ_0, which brings the linear part of the nonadiabatic response over to the left-hand side [only using Eq. (29) for one of the $\partial/\partial t$'s]. This results in an equation similar to the above, except with the Terry–Horton equation on the left-hand side and somewhat different terms on the right.

Transforming Eq. (30) to Fourier k space gives the following mode coupling equation:

$$\frac{\partial\phi_{\mathbf{k}}}{\partial t}=(-i\omega_{\mathbf{k}}+\gamma_{\mathbf{k}})\phi_{\mathbf{k}}+\left(\frac{1+k^2-i\delta_{\mathbf{k}}}{1+k^2}\right)\sum_{\mathbf{k}'+\mathbf{k}''=\mathbf{k}}V_{\mathbf{k},\mathbf{k}',\mathbf{k}''}\phi_{\mathbf{k}'}\phi_{\mathbf{k}''}+\frac{\delta_0}{1+k^2}\sum_{\mathbf{k}'+\mathbf{k}''=\mathbf{k}}V_{\mathbf{k},\mathbf{k}',\mathbf{k}''}(\dot{\phi}^0_{\mathbf{k}'}\phi_{\mathbf{k}''}+\dot{\phi}^0_{\mathbf{k}''}\phi_{\mathbf{k}'})$$

$$-\delta_0\sum_{\mathbf{k}'+\mathbf{k}''=\mathbf{k}}\frac{\hat{\mathbf{z}}\cdot\mathbf{k}'\times\mathbf{k}''}{2(1+k^2)}[\dot{\phi}^0_{\mathbf{k}''}\phi_{\mathbf{k}'}-\dot{\phi}^0_{\mathbf{k}'}\phi_{\mathbf{k}''}+i(k''_y-k'_y)\phi_{\mathbf{k}'}\phi_{\mathbf{k}''}], \tag{31}$$

where

$$\dot{\phi}^0_{\mathbf{k}}=-i\omega_{\mathbf{k}}\phi_{\mathbf{k}}+\sum_{\mathbf{k}'+\mathbf{k}''=\mathbf{k}}V_{\mathbf{k},\mathbf{k}',\mathbf{k}''}\phi_{\mathbf{k}'}\phi_{\mathbf{k}''} \tag{32}$$

and

$$V_{\mathbf{k},\mathbf{k}',\mathbf{k}''}=\frac{1}{2}\frac{\hat{\mathbf{z}}\cdot\mathbf{k}'\times\mathbf{k}''(k''^2-k'^2)}{1+k^2}, \tag{33}$$

the usual Hasegawa–Mima mode coupling coefficient. The frequency and growth rate are given by

$$\omega_{\mathbf{k}}=\frac{k_y}{1+k^2},\quad \gamma_{\mathbf{k}}=\delta_0\frac{k_y^2k^2}{(1+k^2)^3}. \tag{34}$$

Unfortunately, for $k_y>\delta_0^{-1}$ the expansion in $\hat{n}/\phi$ breaks down. Calculating the correct response in this region requires solving the drift-kinetic equation, which is not practical since it evolves on a much faster time scale and since a proper treatment requires three dimensions. One way to avoid this problem is to keep $\delta_0\ll k_{\max}^{-1}$. Typically, we might have $k_{\max}=10$, which would require δ_0 to be no larger than 2% or so, and the maximum growth rate $(4\delta_0/27)$ to be a small fraction of a percent. Not only is this smaller than it should be (for a typical tokamak, $\delta_0\sim0.12$). It is also not practical, since such a small growth rate would cause the time which it takes for a simulation to saturate to become unreasonably large.

We have come up with somewhat of a compromise. We introduce an *ad hoc* nonadiabatic electron model that still incorporates the frequency effects but that remains small for high k:

$$\hat{n}_{\mathbf{k}\omega}=i\delta_0e^{-k^2/k_n^2}(\omega-k_y)\phi_{\mathbf{k}\omega}, \tag{35}$$

where k_n is an undetermined parameter that can be used, along with δ_0, to choose the maximum growth rate and the "nonadiabatic cutoff."

We shall see that the results are sensitive to the cutoff k_n. This seems to discredit the model as an accurate representation of a real plasma. If the high-k modes can have an important impact on the saturated state, then precise calculations of saturated drift wave turbulence cannot be done with *ad hoc* models of the nonadiabatic electron response. That said, we can still learn something from this model, since it is correct at low k and does have the qualitatively correct features in its response to frequency broadening and frequency shifts (including trapped structures).

III. NUMERICAL METHOD

We have developed a Fourier spectral/pseudospectral code[19–22] for solving the model equations discussed in Sec. II. This type of numerical method was chosen for a variety of reasons: First, Fourier methods are a natural choice for homogeneous turbulence simulations. Much of the theoretical work on these problems is done using Fourier analysis.

Second, spectral methods have been used extensively for simulating homogeneous fluid turbulence, where they have been found to be both efficient and accurate.[19,20,23,24]

Spectral and pseudospectral methods represent the spatial dependence of the solution as a series in some set of basis functions. This gives us access to two representations for the solution: the set of amplitudes used in the expansion, and the set of grid values in physical space. There must be a transform method to map these spaces onto each other. We use Fourier modes as our expansion basis, since they are the natural basis for the rectangular periodic grid. (They also happen to be eigenfunctions for the linearized equations, though that is not a requirement of the method.) This allows us to use the fast Fourier transform (FFT), which greatly reduces the number of operations required to perform the transforms.[25]

The pseudospectral method is based on the idea that one should perform the operations needed to advance the differential equation in the most convenient space available. Thus, differential operations are evaluated in Fourier space and nonlinear terms are evaluated in physical space. Our code is structured in exactly this manner. This approach makes the code easy to write and modify since it is similar to the way the physicist thinks about the problem. Unfortunately, for nonlinear problems this can lead to the so-called "aliasing" instability. This instability is due to the fact that the nonlinear terms generate higher frequencies than can be resolved on the grid. When this data is transformed back into Fourier space, the energy in these high-frequency modes is misinterpreted as belonging to certain low-frequency modes (which are the "aliases" of the high-frequency modes since the two cannot be distinguished on the fixed grid). Fortunately, the pseudospectral algorithm can be modified in a straightforward manner (using a conservative smoothing operation) to remove these aliasing problems. This "dealiasing" effectively turns the code into a spectral code. (In terms of code efficiency, this is not the optimal way to write a spectral code. The order of the operation count is not affected but the multiplying constant is.)

The equations are advanced in time using a high-order Runge–Kutta adaptive time-step algorithm. Although these methods have larger memory requirements than simpler methods, we have found that they allow a considerably larger time step while maintaining good accuracy.

Typically, our simulations used an 80×80 or 128×128 grid, with a box size of 20π on each side (so $k_{\min}=0.1$). The code was tested by checking both local conservation properties (making sure that fluid marker particles traveled along contours of constant ρ, and that such contours were area preserving) and global conservation properties (conservation of total energy and enstrophy); and by testing its ability to reproduce an exact nonlinear solution. The error tolerance for the adaptive time-stepping routine was chosen so that the energy and enstrophy moments were conserved to several (six to ten) places. For details of these tests, see Ref. 26.

IV. HASEGAWA–MIMA SIMULATIONS

Before we try to understand the turbulent evolution of Eq. (30), it is instructive to spend some time studying the Hasegawa–Mima equation, Eq. (1). In this section we briefly discuss the evolution of isolated structures. We then examine decaying Hasegawa–Mima turbulence, in which long-lived coherent structures are seen to evolve from noisy random initial conditions.

A. Isolated structures

The inviscid Hasegawa–Mima equation possesses a family of exact traveling wave solutions [of the form $\phi(x,y-ct)$], which are strong enough to trap particles.[17,27,28] The simplest member of this family is a dipole vortex type solution, usually called a *modon*. These structures have been studied by many authors. However, they are rarely observed in simulations of two-dimensional turbulent systems. There are several reasons why this is so: They require a large amount of energy to form and they appear to be unstable to long-wavelength nonsymmetric perturbations.[26,29] Also, if the model includes nonadiabatic electron effects, these will act to damp the modons. Thus our interest in studying modons is limited to using them as a test of the code. These tests show that the code converges in both the L_2 sense and in the measurement of the modon velocity, with convergence in the latter being faster.[26]

The second type of trapped structure is that created by a large monopole fluctuation. There are no exact monopole solutions of the form $\phi(x,y-ct)$ because the monopoles interact strongly with the linear modes. These linear modes have phase velocities in the range $0<\omega/k_y<1$. Modons do not interact with these waves because their velocities complement this range. This is made possible by the very strong interaction between the two lobes of the dipole. An isolated monopole has no such mechanism for self-propulsion. It moves with a y velocity, c_y, in the range $0<c_y<1$—it is resonant with the linear wave spectrum. As it moves through the plasma, it thus loses energy via a Čerenkov emission process. As it loses energy it must move in the x direction in order to conserve ρ in the trapped interior region.

The questions are: How long would such a structure last? and How fast does it give up energy to the linear waves and move in x? Although it seems as if this would be an analytically tractable problem, assuming the x velocity, c_x, is small, it has not, to our knowledge, been solved. The problem is greatly complicated by the fact that the solution in the outer region is an outgoing wave.

Figure 1 illustrates the evolution of an initially symmetric monopole fluctuation. Figure 2 illustrates the trajectory of a fluid particle trapped in that monopole. Initially, there is a short relaxation period. During this time the monopole gains a small asymmetric component and its x and y velocities change slightly from their initial values (these velocities are given roughly by the average slopes of the curves in the x-t and y-t plots in Fig. 2). After this quick adjustment, the monopole seems to settle into a qua-

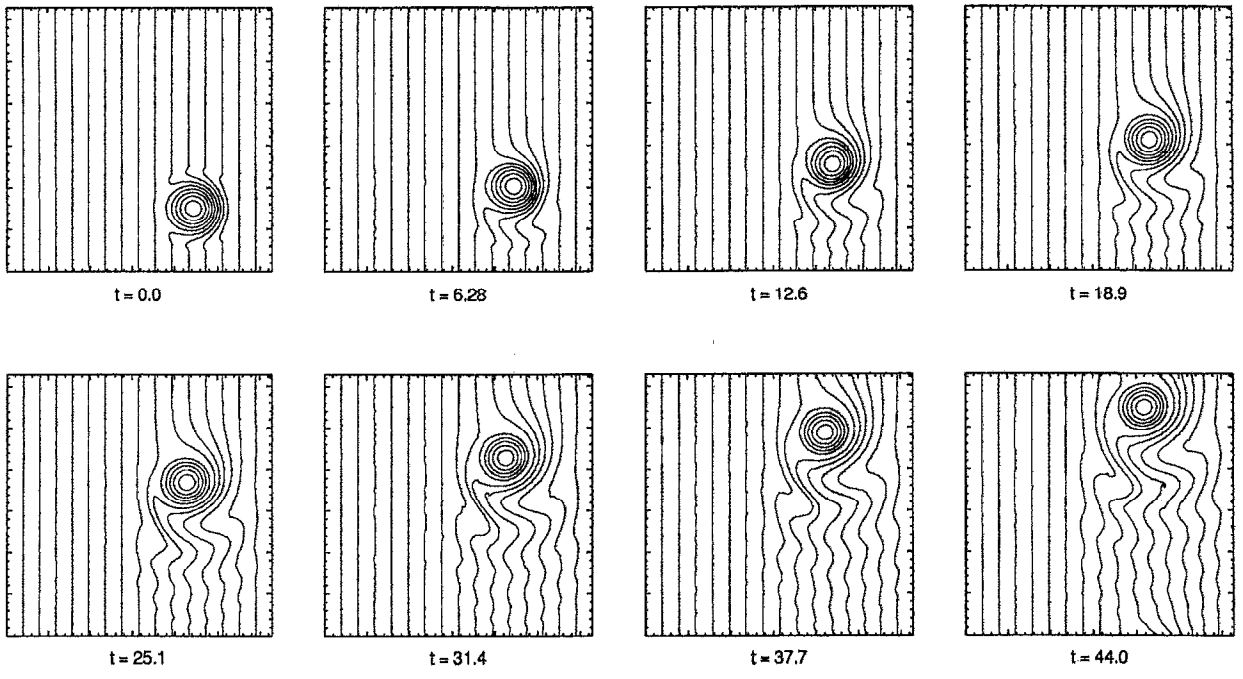

FIG. 1. Evolution of an isolated monopole vortex. The contour lines are lines of constant ρ. The box size is $20\pi \times 20\pi$.

sistationary state moving with a constant x and y velocity with, in this case, $0 < |c_x| \ll c_y < 1$. There is also a trailing wake created behind the monopole as it gives up energy to the waves via Čerenkov emission.

Dozens of such monopoles have been studied, varying the monopole radius and average electric field. As long as their radius was not too small, in which case dispersion quickly destroyed them, they behaved in a manner similar to that described above. Both Gaussian profiles and polynomial profiles were used as initial conditions. Monopoles of roughly the same size and electric field led to very similar histories, regardless of the details of their profile. The x velocity was usually fairly small, and the y velocity was usually in the range $0.5 < c_y < 1.0$. The fact that the x velocity was generally found to be quite small indicates that the monopole lifetime, though not infinite, can be very long (roughly $\phi_{\max}/c_x$).

Due to the periodic boundary conditions, the box eventually begins to fill with waves excited by the monopole. When these waves get sufficiently large they will, of course, interfere with the monopole's evolution.

Two trends were observed: The monopole lifetime increased (i.e., c_x decreased) both as its radius increased and as the average electric field increased. The first trend is to be expected. As the radius of the structure increases, its lifetime should increase. The process of losing energy to the waves occurs through dispersion. In fact, were it not for the dispersive term in the equation, any symmetric

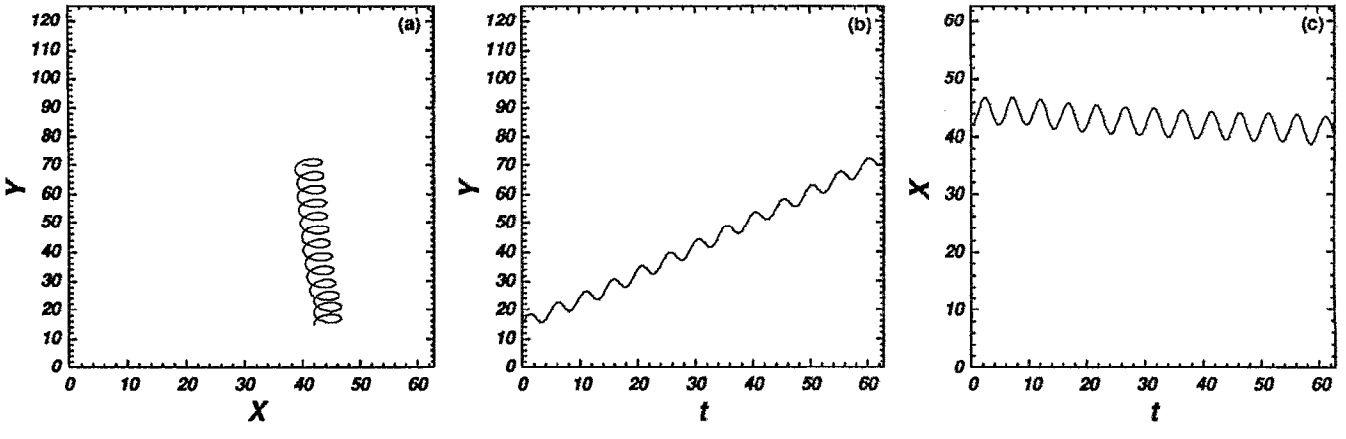

FIG. 2. Trapped particle trajectory for a fluid particle trapped in the monopole shown in Fig. 1. Shown are (a) the actual trajectory, (b) the time dependence of the y position, and (c) the time dependence of the x position.

TABLE I. Input parameters for the decaying turbulence runs.

Input parameter	Value
$H_x=H_y$	20π
k_{max}	6.3
ϕ_0	0.15
k_l	2.0
k_u	2.5
ν_4	0.003

structure would be an exact solution to the equation, since a symmetric function trivially annihilates the equation's vector nonlinearity. Making the structure large makes the dispersive term small. The second trend is not so easy to understand. We note that the stronger electric field means that the inner particles are trapped more strongly and that the rotational velocity of the structure is higher. This tends to make the structures more circular, which may, in turn, affect the rate of dispersion.

In summary, the monopole solution can be very long lived, and appears to be quite robust. Various perturbations such as viscosity, nonadiabatic electrons, and random noise have been studied. The isolated monopole is only weakly affected by these various perturbations.

B. Decaying turbulence

Next we will examine some runs in which the damped Hasegawa–Mima equation evolves from noisy initial conditions, leading to a turbulent decay. Table I describes a typical decay run. The initial conditions are given by

$$\phi_{\mathbf{k}}(t=0)=\begin{cases}\phi_0 e^{-i\alpha(\mathbf{k})} & k_l<k<k_u,\\ \epsilon, & \text{otherwise},\end{cases} \tag{36}$$

where $\alpha(\mathbf{k})$ is a uniformly distributed random number in the range $0<\alpha(\mathbf{k})<2\pi$. Figure 3 shows the energy and enstrophy histories for this run. Observe that the energy drops by a moderate fraction of its initial value while the enstrophy drops to nearly zero, as expected from the discussion in Sec. II.

Figure 4 illustrates the evolution of the energy spectrum. Initially there is a rapid transfer of energy from the original high-k annulus to low k. After this the system settles into its quasisteady decay. In this region we observe that the slope of the energy spectrum is steeper than k^{-3} (the slope predicted by the two-dimensional version of

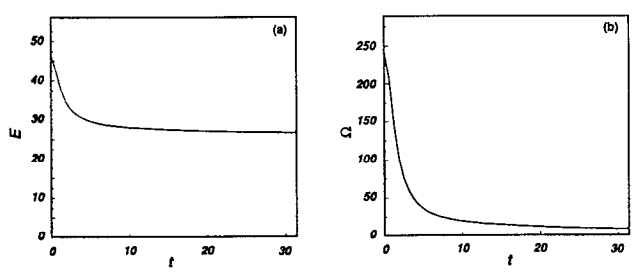

FIG. 3. Energy and enstrophy relaxation for the decaying turbulence run.

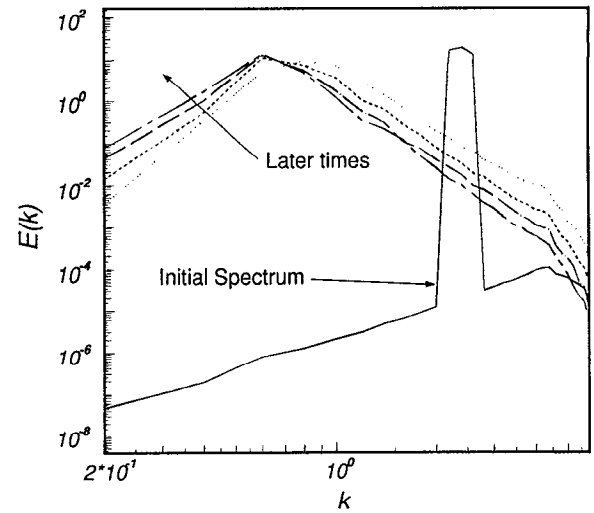

FIG. 4. Evolution of the isotropic energy and enstrophy spectra for the decaying turbulence run.

Kolmogorov's cascade theory)—in fact, a bit steeper than k^{-5}. The low-k spectrum never reaches a steady shape. Energy continues to build up at the lowest wave numbers while the remaining modes slowly diminish.

Figure 5 shows a series of contour plots illustrating the evolution of ρ following the initial, fast decay. Regions of closed contours may be seen in these plots. These regions represent prospective trapped structures. Several of these regions are shaded, and it can be seen that these are indeed coherent.

The large structure in the lower left quadrant of the first frame can be tracked throughout the evolution. In the final frame we see it disappearing. It is interesting to note the mechanism by which it disappears. Unlike vortices seen in two-dimensional Navier–Stokes simulations, where the vortex count decreases due to vortex mergers, this structure appears to have just gone away. There are two mechanisms by which this can occur. One is that the structure can move in the x direction. Since $\rho=x-\phi+\nabla_\perp^2\phi$ must be nearly conserved at its center, the motion in x causes the size of the fluctuation, and thus the size of the trapped region, to decrease. This mechanism has already been mentioned with regards to the Čerenkov emission of waves by isolated structures. Motion in x can also be caused by convection, usually due to one or more other structures. A second detrapping mechanism is for nearby lines of constant ρ to move in the x direction and reconnect with the constant ρ lines of the vortex. This can occur when a large untrapped fluctuation that is localized in the y direction comes in close proximity to the trapped structure. Figure 6 illustrates this idea.

Both of these mechanisms appear to play a role in the disappearance of the structure in question. Its center has moved from $x=23$ to $x=13$. However, it is still a considerable distance from its "equilibrium" position (the shaded vertical strip at the extreme left of the last frame of Fig. 5)—the position with the same value of ρ when there are no fluctuations in the system. At least part of the reason for

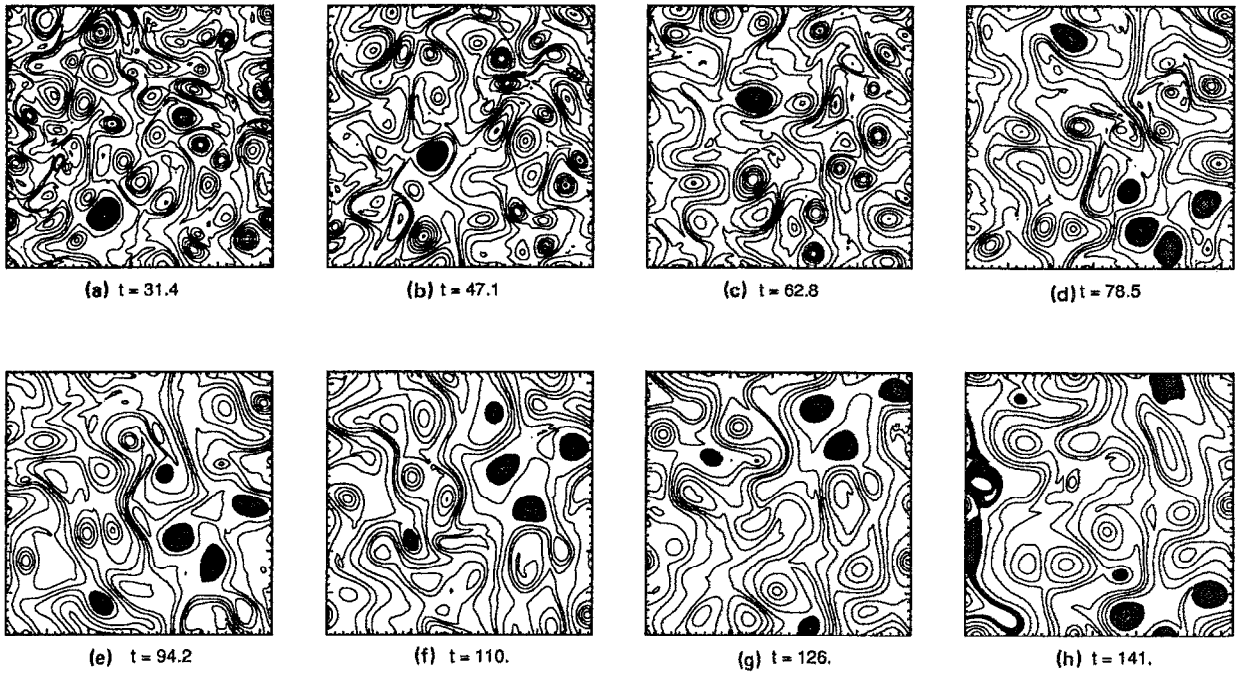

FIG. 5. Contours of constant ρ during the quasisteady stage of the decaying turbulence run. The box size is $20\pi \times 20\pi$.

it becoming untrapped is the large untrapped perturbation above it (shown in the lower left of the last frame).

These mechanisms for detrapping can also serve as mechanisms for trapped structure formation. Compared with vortex–vortex mergers, these detrapping mechanisms seem quite nonviolent, and are probably more reversible.

Four other vortices are shaded in the last five frames of Fig. 5, starting in the lower right quadrant of Fig. 5(d). Note the remarkable similarity between their relative locations in the fourth and last frames. This is indicative of the very narrow frequency spectrum of the "turbulence" once the decay reaches this point. Unfortunately, the frequency spectrum cannot be quantitatively measured for these decay runs, since the average quantities are changing much too quickly. However, we can make some qualitative comments. The decay runs tend to be characterized by localized structures, slowly interacting, coalescing, and moving to larger scales. During this slow evolution, the motion of the various large vortices is very uniform. They all move with a y velocity very near

$$\frac{E}{E+\Omega} = \frac{1}{1+\Omega/E} = \frac{1}{1+k_*^2},$$

and with very little x motion. Except during a rare interaction, they remain basically circular. This motion is extremely coherent, and deviations from this coherent motion occur on a time scale much longer than ω_{*e}. Qualitatively speaking, the width of the frequency spectrum is much smaller than the frequency: $\Delta\omega \ll \omega$.

Coherence may also be checked by placing marker particles, which move with the fluid velocity, in the trapped

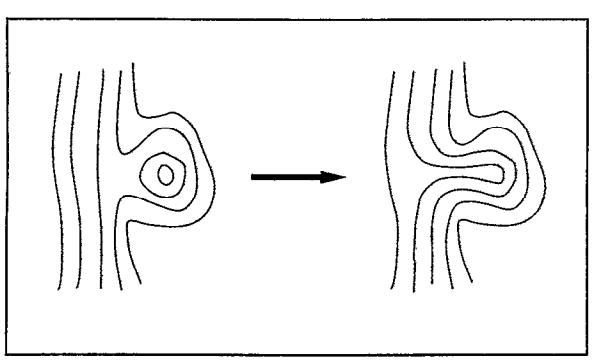

FIG. 6. Detrapping of a vortex by reconnection with nearby ρ lines.

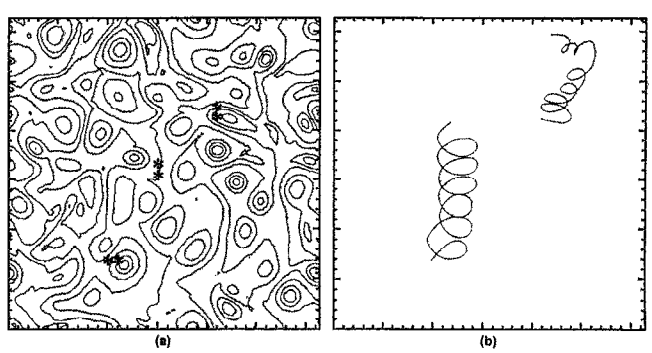

FIG. 7. Marker particle trajectories. Shown are (a) the initial positions (the asterisks) of several particles (on a graph of ρ) and (b) the trajectories of two of these particles. The box size is $20\pi \times 20\pi$.

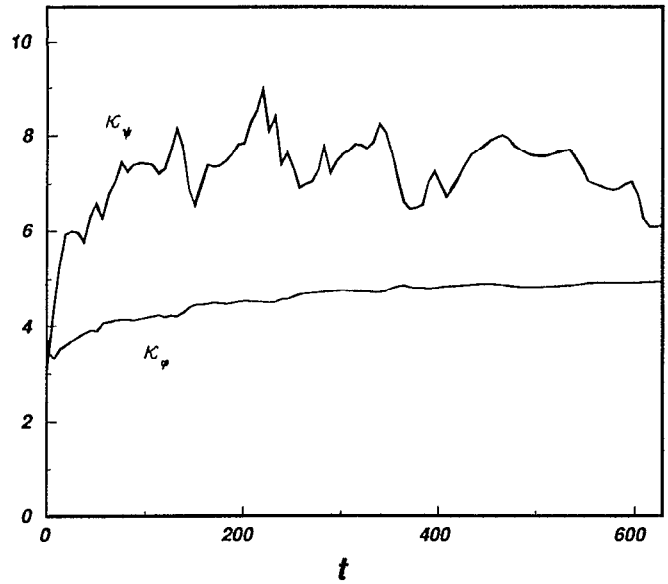

FIG. 8. Potential and vorticity kurtoses for the zero-gradient run.

regions and integrating the particle trajectories simultaneously with the fields. Figure 7(a) shows the initial positions of six such markers, indicated by the *'s. The initial field is the same as that shown in the first frame of Fig. 5. Figure 7(b) shows the trajectories of two of the marker particles from $t=31.4$ to $t=53.4$. The trajectory on the left is that of one of two particles that were placed in the structure discussed above. Both of these particles were trapped. Note the very regular motion of this particle. Its trapping period is about 7 (times ω_{*e}^{-1}). The trajectory on the right is much more irregular, due to the fact that the vortex in which the particle is trapped becomes untrapped at around $t=50$. The two particles shown in the center of Fig. 7(a) are purposely placed in an untrapped region. Their trajectories (not shown) quickly diverge. Note, however, that the divergence is pseudo-one-dimensional, since both particles must stay near their constant-ρ line.

Many of the observations made above are due to the explicit linear dependence of ρ on x, a direct consequence of the finite density gradient. This is seen to affect the solutions in many ways. The average value of x must be conserved, there are no exact monopole solutions, there are new ways in which trapped structures can be born and destroyed, and there are limitations to how particles can diffuse. It is thus of interest to compare the above decay run with an identical run in which there is no density gradient. The Hasegawa–Mima equation then becomes

$$\left(\frac{\partial}{\partial t}+\hat{\mathbf{z}}\times\nabla_\perp\phi\cdot\nabla_\perp\right)(\phi-\nabla_\perp^2\phi)+\nu\nabla_\perp^4\phi=0. \tag{37}$$

This equation is solved for the same initial conditions, etc., as used above. The evolution of the total energy and enstrophy for this zero-gradient run is nearly identical to that shown in Fig. 3. The evolution of the energy spectrum is also similar to that in Fig. 4, except that the high-k slope is somewhat steeper (about k^{-6}) than is the case with the finite gradient.

In order to make contact with previous work on similar zero-gradient problems[14] we calculate the kurtosis of the field fluctuations, an important statistic in studying intermittency. The kurtoses for the potential and the fluid vorticity, $\nabla_\perp^2\phi$, are defined as

$$\kappa_\phi\equiv\frac{L^2\int\phi^4\,d^2x}{(\int\phi^2\,d^2x)^2} \tag{38}$$

and

$$\kappa_\psi\equiv\frac{L^2\int(\nabla_\perp^2\phi)^4\,d^2x}{[\int(\nabla_\perp^2\phi)^2\,d^2x]^2}, \tag{39}$$

where L^2 is the area of the domain. If the spatial scale of the fluctuations had a Gaussian distribution, then the kurtosis would be equal to 3. The kurtosis is greater than 3 if the distribution of fluctuations has a long tail, which results in a larger than Gaussian probability of seeing a very large fluctuation. For instance, an intermittent field with a few widely separated, large fluctuations will have a kurtosis much larger than 3.

Figure 8 shows the spatial kurtosis of the potential and the fluid vorticity for the zero-gradient run. We see a trend similar to that noticed by McWilliams:[14] the kurtosis of the streamfunction (the potential, in our case) remains close to 3 while the kurtosis of the vorticity grows significantly larger than 3. For comparison, Fig. 9 shows the same quantities plotted for the finite gradient run. The kurtosis of the potential again remains near 3 throughout the simulation. The kurtosis of the vorticity initially grows, as in the zero-gradient case. However, this seems to be a transient effect, with the finite gradient kurtosis returning to approximately 4 after the first 200 drift periods.

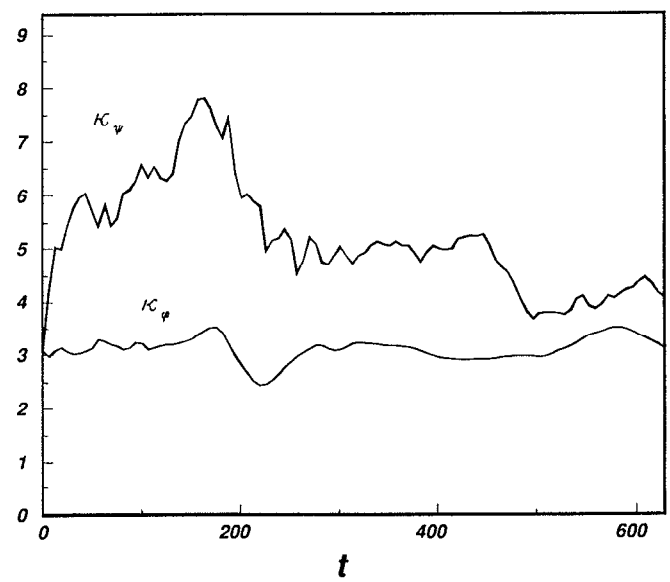

FIG. 9. Potential and vorticity kurtoses for the finite-gradient run.

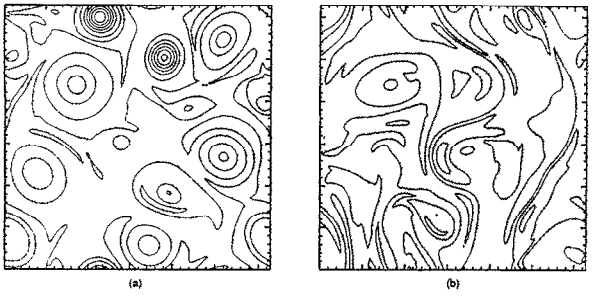

FIG. 10. Comparison of the vorticity contours for zero (left) and finite (right) gradient runs. The box size is $20\pi \times 20\pi$.

This difference is due, in part, to the Čerenkov emission process, which causes the space between trapped vortices to fill up with waves. The kurtosis cannot distinguish between the fluctuations due to waves and those due to trapped structures. So, although it may be a good measure of intermittency, it is not a good trapped structure diagnostic.

Figure 10 shows the contours of the vorticity function at the end of these runs. We see that they are, indeed, quite different. The vorticity for the zero-gradient run is concentrated in localized vortex structures, while the vorticity for the finite gradient run is much less organized.

The vorticity, however, is not the correct quantity to measure if we are seeking to identify trapped structures. It *is* useful, since it indicates the local rotation rate of the fluid, and also gives us an indication of where energy is being dissipated. But with regard to trapped structures, ρ is really the more meaningful quantity, as its contours represent the actual lines along which particles move. For the zero-gradient runs, this quantity is simply

$$\rho = \nabla_1^2 \phi - \phi.$$

Figure 11 shows the contours of ρ for both runs. In neither case is the field extremely intermittent. Indeed, the kurtosis for the function $\nabla_1^2\phi - \phi$, which in both cases represent the fluctuation in ρ, always tends to be very near 3. This is not surprising, since the average k vector tends to be relatively small, making $\nabla_1^2\phi \ll \phi$, so that the statistics of ρ will be very similar to those of ϕ. Thus we see that the trapped structures in both cases tend to not be very isolated. However,

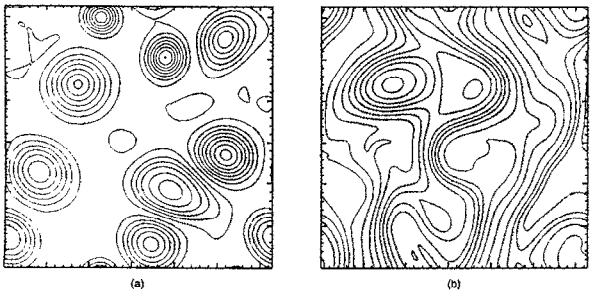

FIG. 11. Comparison of the ρ contours for zero (left) and finite (right) gradient runs. The box size is $20\pi \times 20\pi$.

TABLE II. Effects of varying the strength of the nonadiabatic electron term, as represented by $\gamma_{\max}$. All runs had $H_x = H_y = 20\pi$, $k_{\max} = 3.9$, $\nu_4 = 0.05$, and $k_n = 1.0$.

$\gamma_{\max}^L$	0.025	0.04	0.075	0.10
E	17.5	11.0	6.1	4.7
Ω	5.5	5.7	4.5	4.1
$k_* = \sqrt{\Omega/E}$	0.56	0.72	0.85	0.92
$(\nabla\phi)_{\text{rms}}$	2.7	2.4	2.3	2.2

we definitely see more trapped structures in the zero-gradient run. This is surely due, at least in part, to the additional detrapping mechanisms available in the finite gradient case.

V. SATURATED TURBULENCE

The Hasegawa–Mima simulations led to some interesting observations: that very long-lived trapped structures could develop in decaying turbulence, and that the frequency spectrum of the fluctuations was quite narrow. Both of these observations are long time-scale observations, however, and thus we should expect the nonadiabatic electrons to have a strong effect on them.

In this section we study the saturated turbulence which develops when the nonadiabatic electrons are included in the problem. Our main focus will be to see if the trapped structures, which were so prominent earlier, still play a role; and to see what type of effect our nonadiabatic electron term has.

A. Frequency spectrum and energy saturation

Although the energy analysis of Sec. II is not exact for our model equation, the effects of spectral broadening and shifting are included in an approximate way. This fact greatly complicates our view of what is happening. In the Terry–Horton model the picture is fairly clear: there is a source of energy at low k due to the nonadiabatic electrons, and there is a sink of energy at high k due to ion viscosity. This allowed Terry and Horton to make a rather general prediction of the circumstances under which the system would saturate. Arguing that if the energy grew large enough, mode coupling would drive the system toward equipartition,[30] they showed[5–7] that the system would saturate if

$$\gamma_t \equiv \sum_{\mathbf{k}} (\hat{\gamma}_{\mathbf{k}}^L - \nu_k) < 0.$$

Thus, as one increases δ_0, approaching the critical value where $\gamma_t = 0$, the saturation energy is expected to increase without bound.

Such a simple picture does not work for our model. Increasing δ_0 affects more than just the linear growth rate. It increases the strength of the nonadiabatic electron term in general, which may be a sink as well as a source. It also modifies the spectrum, and thus $\bar{\omega}_{\mathbf{k}}$ and $\Delta\omega_{\mathbf{k}}$.

Table II illustrates this point quite dramatically. This table compares four runs whose only difference in input was the value of $\gamma_{\max}^L$, the maximum linear growth rate

TABLE III. Effect of input parameters on saturation energy, enstrophy, and electric field.

Run	ν_4	$\gamma^L_{\max}$	k_n	E	Ω	$\nabla\phi$
	0.05	0.04	∞	10.0	2.3	1.5
	0.05	0.04	1.0	11.0	5.7	2.4
	0.05	0.04	0.4	18.0	7.8	3.2
	0.05	0.040	∞	10.0	2.3	1.50
	0.05	0.075	∞	3.6	2.2	1.55
A[a]	0.05	0.100	∞	2.4	1.9	1.35
	0.05	0.025	1.0	17.5	5.5	2.7
	0.05	0.040	1.0	11.0	5.7	2.4
	0.05	0.075	1.0	6.1	4.5	2.2
B[a]	0.05	0.100	1.0	4.7	4.1	2.0
	0.05	0.025	0.4	25.0	9.0	3.4
	0.05	0.040	0.4	18.0	7.8	3.2
	0.05	0.075	0.4	15.0	8.0	3.1
	0.025	0.04	∞	7.0	2.2	1.8
	0.050	0.04	∞	10.0	2.3	1.5
	0.075	0.04	∞	13.0	2.0	1.8
	0.100	0.04	∞	14.0	1.6	1.7
	0.010	0.04	1.0	9.2	6.7	2.6
	0.025	0.04	1.0	10.5	6.2	2.6
	0.050	0.04	1.0	11.0	5.7	2.4
C[a]	0.075	0.04	1.0	11.0	4.7	2.4
	0.100	0.04	1.0	11.5	4.5	2.4
	0.010	0.04	0.4	19.0	11.0	3.3
	0.025	0.04	0.4	18.0	8.8	3.0
	0.050	0.04	0.4	18.0	7.8	3.2
D[a]	0.075	0.04	0.4	17.5	6.8	3.2
	0.100	0.04	0.4	17.0	6.7	3.0

[a]For runs A–D see Table IV, respectively.

(which is directly proportional to δ_0). There are two notable results: First, as $\gamma^L_{\max}$ was increased, the saturation energy *decreased*! Second, the root mean square (rms) electric field was relatively constant due to the fact that, as the energy went down, the average k vector went up.

The relatively weak dependence of the electric field on $\gamma^L_{\max}$ is further explored in Table III. These runs are identical to those listed in Table II, except for the variations of $\gamma^L_{\max}$, ν_4, and k_n shown. We see that the electric field also depends only weakly on the viscosity. The only input value upon which the saturated electric field depends strongly is the nonadiabatic cutoff, k_n.

The strong dependence of the saturation level on k_n is understandable. The high-k modes tend to have very broad frequency spectra, and thus to have negative nonlinear growth rates. By limiting the effect of the nonadiabatic electrons to low k, we are removing a sink of energy.

In order to further study the effect of k_n, we show more detailed spectral information for four of these runs in Table IV. These runs correspond to the footnoted runs in Table III. Their differences are summarized in Table V. They are presented in order of increasing average (rms) electric field. Shown in Table IV are the mode energy, $E_{\mathbf{k}}$, linear

TABLE IV. Detail of the frequency characteristics for runs A–D.

Run	(k_x,k_y)	$E_{\mathbf{k}}$	$\omega_{\mathbf{k}}$	$\Delta\omega$	$\delta\omega$	$\gamma^{\rm NL}_{\mathbf{k}}/\delta_0$
A	(0.0,0.6)	0.076	0.44	0.042	0.030	0.043
	(0.6,0.0)	0.009	0	0.144	0.009	−0.015
	(0.0,1.1)	0.007	0.50	0.205	−0.097	0.108
	(1.1,0.0)	0.002	0	0.343	0.001	−0.053
B	(0.0,0.9)	0.034	0.50	0.235	−0.105	0.079
	(0.9,0.0)	0.019	0	0.284	−0.006	−0.045
	(0.0,1.1)	0.016	0.50	0.309	−0.167	0.072
	(1.1,0.0)	0.010	0	0.347	−0.011	−0.054
C	(0.0,0.5)	0.194	0.40	0.079	−0.0036	0.028
	(0.5,0.0)	0.112	0	0.10	0.009	−0.009
	(0.0,1.1)	0.007	0.50	0.400	−0.181	0.040
	(1.1,0.0)	0.004	0	0.40	−0.003	−0.071
D	(0.0,0.6)	0.252	0.44	0.158	−0.043	0.041
	(0.6,0.0)	0.194	0	0.166	−0.006	−0.020
	(0.0,1.1)	0.008	0.50	0.603	−0.25	−0.068
	(1.1,0.0)	0.007	0	0.418	−0.001	−0.079

frequency, $\omega_{\mathbf{k}}$, linewidth, $\Delta\omega$, frequency shift,

$$\delta\omega \equiv \bar{\omega}_{\mathbf{k}} - \omega_{\mathbf{k}},$$

and a measure of the nonlinear growth rate,

$$\frac{\gamma^{\rm NL}_{\mathbf{k}}}{\delta_{\mathbf{k}}} = -\frac{1}{1+k^2}\left[\Delta\omega^2 + \bar{\omega}(\bar{\omega}-k_y)\right].$$

The factor $\delta_{\mathbf{k}}$ is scaled out so that this is purely a measure of the effect of the frequency width and shift, depending only on $\delta_{\mathbf{k}}$ through the changes it causes to the spectrum. Values are given for the k vectors with the highest energy along with its counterpart on the k_x axis. Values are also given for two higher-k modes.

Run A has the lowest electric field of all those shown in Table III. In this case, we see that the frequency spectrum is fairly narrow relative to the mode frequency. For the strongest mode in the system, $\Delta\omega/\omega < 10\%$. Also, the spectral characteristics are quite anisotropic. The k spectrum is much larger along the k_y axis, which we might expect, since the linear growth rate is largest there. But the linewidths tend to be broader near the k_x axis, even though the energy in these modes is smaller. These observations are reflected in the nonlinear growth rate, which is positive along the k_y axis, and negative along the k_x axis. The deviations of this growth rate from the linear one are mostly due to the broadening term—the shift $\delta\omega$ is not sufficiently large to have much of an effect. The average frequency, $\bar{\omega}_{\mathbf{k}}$, appears to drop off somewhat faster than the linear growth

TABLE V. Input differences for runs A–D.

Input parameter	run A	run B	run C	run D
$\gamma^L_{\max}$	0.10	0.10	0.040	0.040
ν_4	0.05	0.05	0.075	0.075
k_n	∞	1.00	1.000	0.400

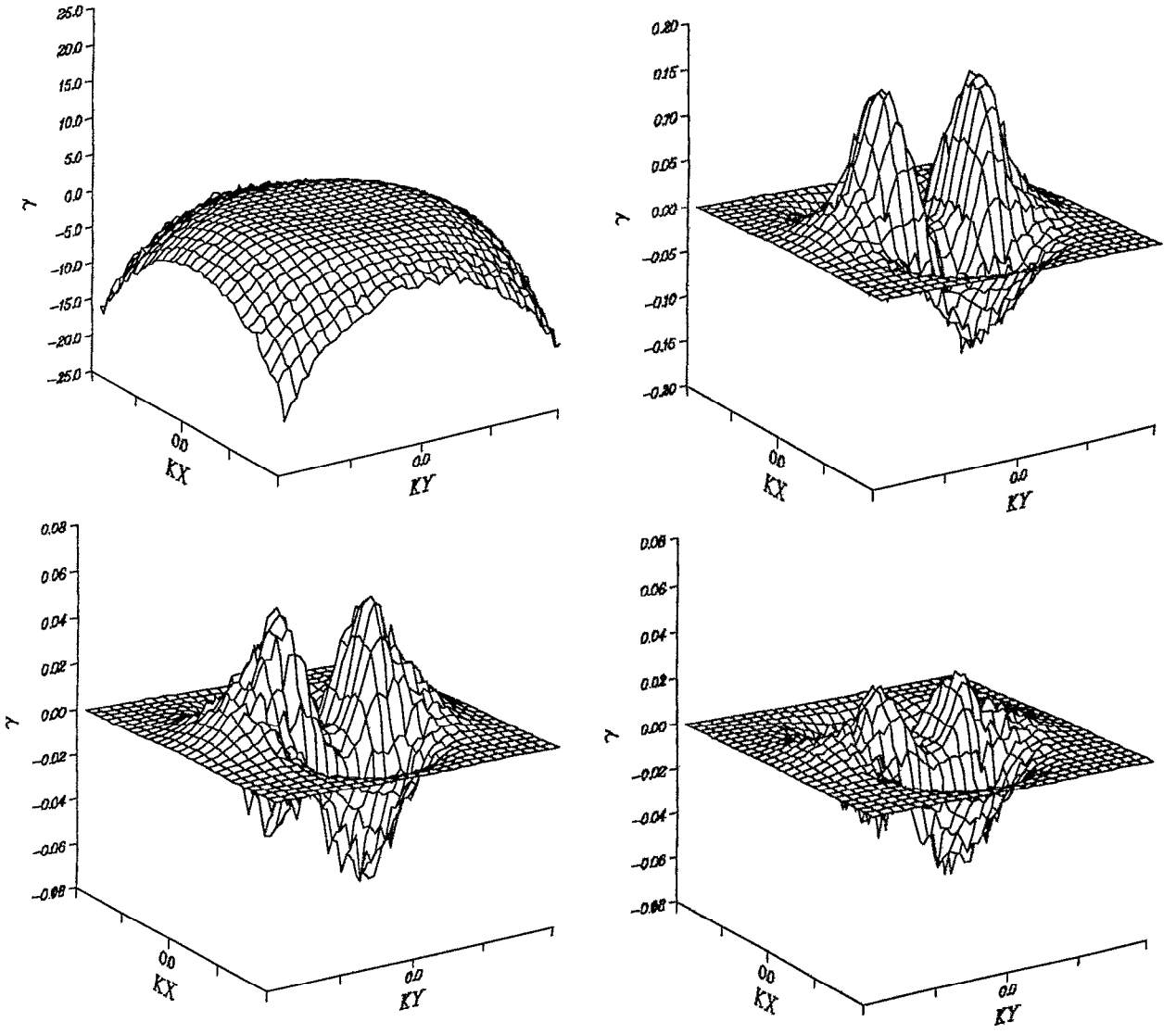

FIG. 12. Nonlinear growth rate, γ_k^{NL}, for runs A–D.

rate, but it is difficult to draw any firm conclusions, since the precise value of this average becomes difficult to determine when the spectrum is very broad.

Run B was identical to run A, except that k_n was decreased to $k_n = 1$. We see that the corresponding increase in the average electric field has resulted in broader linewidths, with the strongest mode now having $\Delta\omega/\omega \approx 50\%$, and a more isotropic k spectrum. This is again reflected in the nonlinear growth rate, which is generally smaller than before.

For run C, the maximum linear growth rate was decreased to $\gamma_{\max}^{L} = 0.04$ and the viscosity was increased slightly. This resulted in an average total energy of over twice that in run B. The electric field, however, changed only slightly. The linewidth for the strongest mode dropped back to around 20%. The higher-k modes were still fairly broad. The k spectrum was slightly more isotropic than it was for run B, but not much different. The narrowing of the frequency spectrum caused some of the nonlinear growth rate terms to increase.

Finally, k_n was decreased to 0.4 for run D, resulting in an average electric field of over 3.0. The linewidth of the strongest mode was slightly over 33%, and the high-k modes were quite broad. The k spectrum was nearly isotropic.

The nonlinear growth rate is an excellent measurement with the characteristics of the frequency spectrum, since it ties in directly with the energy balance for the model. Table IV gives measurements of the nonlinear growth rate for only a few modes, as it is very expensive to calculate the frequency spectrum. However, we can use Parseval's theorem to calculate the nonlinear growth rate directly in the simulation code:

$$\gamma_k^{NL} = -\frac{\delta_k}{E_k}\frac{1}{T}\sum_{t=0}^{T}\frac{\partial\phi_k^*}{\partial t}\left(\frac{\partial\phi_k}{\partial t} + ik_y\phi_k\right). \tag{40}$$

Equation (40) is used in the code to calculate the nonlinear growth rate. Figure 12 shows the average nonlinear growth rate for runs A–D. In the case of run A, we see just how strong a damping force the nonadiabatic electrons can be—the nonlinear damping at the edge of the spectrum is so large ($\approx$5–20) that the details of the low-k growth rate are completely invisible on the same scale. In the other figures the peak growth rate is not much different from the linear value, being moderately lower for the case of run D. Another important feature of these plots is the large anisotropy at small to moderate wave numbers, with strong damping at low k along the k_x axis, and a positive growth rate extending out to fairly high k along the k_y axis.

The spectral data indicates that the linewidths for the strongest modes were only moderately broad, with the width increasing as the electric field and the linear growth rate were increased. While these linewidths are not insignificant, they are also not as wide as some experimental observations would lead us to expect. Tokamak discharges are often characterized as having frequency spectra with $\Delta\omega \gtrsim \omega$. Note that we are not implying that this simple model should reproduce the details of core turbulence in a tokamak. (Also, note that there are many uncertainties in the experimental measurements, and it is not impossible that the broad spectral measurements might be due to an effect other than the drift wave fluctuations.) However, if the broad frequency spectrum is purely an artifact of the nonlinear coupling, then our model ought to reproduce this feature. Also, such broad linewidths have been observed in other drift wave simulations.[4,7] Thus we were somewhat curious as to why our measured widths were not broader. The answer is that such broad widths are not possible with this nonadiabatic electron model. Let us calculate the frequency broadening required to stabilize a mode, assuming that the shift is negligible (which is supported by the above data). We then have

$$\gamma_{\mathbf{k}}^{\mathrm{NL}} = -\frac{\delta_{\mathbf{k}}}{1+k^2}\left[\Delta\omega_{\mathbf{k}}^2 + \bar{\omega}_{\mathbf{k}}(\bar{\omega}_{\mathbf{k}} - k_y)\right] = 0,$$

or, setting $\bar{\omega}_{\mathbf{k}}$ equal to $\omega_{\mathbf{k}}$,

$$\Delta\omega_{\mathbf{k}}^2 = -\omega_{\mathbf{k}}(\omega_{\mathbf{k}} - k_y) = k^2\omega_{\mathbf{k}}^2.$$

Thus we see that a mode will be damped if $\Delta\omega_{\mathbf{k}} > k\omega_{\mathbf{k}}$. Our simulations show that the energy containing modes are usually in the range $0.5 < k < 1.0$. Some of these modes must have a positive growth rate in order for the system to maintain a saturated state. These modes, then, cannot have the broad spectrum characteristic of the experiments.

It is important to note that the problem here lies with our model for the nonadiabatic electrons, not with our treatment of the ions. The results are, indeed, very sensitive to changes in the nonadiabatic electron model, as is reflected by the strong dependence of the saturated state on the value of k_n. It is not difficult to imagine that a completely different electron model, due to a different instability mechanism, might lead to broader spectra.

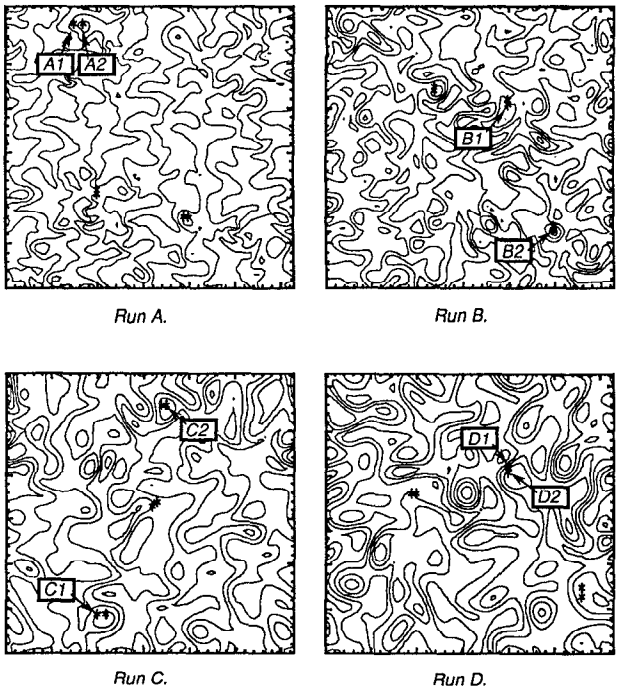

FIG. 13. Contours of ρ for the saturated turbulence runs, runs A–D, with marker particles (*). The box size is $20\pi \times 20\pi$.

B. Trapped structures

The frequency and wave number spectra tell us nothing explicit about whether or not monopole trapped structures exist in the system. Both monopoles and waves have dispersion relations that are very similar:

$$\omega_{\mathbf{k}} = k_y/1+k^2, \quad \text{linear waves,}$$
$$\omega_{\mathbf{k}} = ck_y, \quad \text{monopole vortices,}$$

where $c \sim 1/(1+\bar{k}^2)$, $\bar{k}$ being an average wave vector for the monopole. The ω spectrum of an isolated monopole is discrete, but if the system has many monopoles, each having a different velocity and size, then the frequency spectrum will be broadened. The broadening is further enhanced by monopole–monopole interactions. The difference between a broad spectrum of waves and a chaotic system of monopoles lies in the phase coherence of the modes. This information is completely absent from the spectrum.

The moderately broad spectra observed in runs A–D thus do not preclude the existence of trapped structures. One would expect, however, that the monopole lifetime would decrease as the spectrum broadened.

Figure 13 shows contours of constant ρ for runs A–D after the turbulence has saturated. The asterisks indicate the initial positions of marker particles that were evolved with the flow. Some closed contours can be seen in all four cases, though the number of such and the size of the enclosed regions increase dramatically as the rms electric field increases. Figure 14 shows the trajectories of some of these particles for 12.5 drift periods.

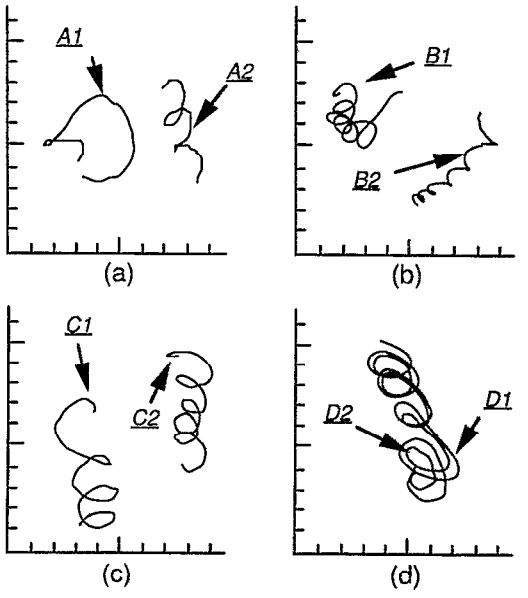

FIG. 14. Particle trajectories for the particles labeled in Fig. 13.

For run A, with a rms electric field of only 1.5, the potentially trapped regions are nearly lacking. Clearly, the majority of the fluid is not trapped in this case. Figure 14(a) shows the trajectories of two of the marker particles, labeled A1 and A2 in Fig. 13. Although the two particles were initially in close proximity to each other, their trajectories quickly diverged as A1 was not trapped and A2 was. (The trajectories have been displaced for clarity.) The trapping period for particle A2 is approximately six drift periods.

Figure 14(b) shows the trajectories of the two particles labeled B1 and B2 in Fig. 13. Particle B1 appears to have been initially untrapped. Actually, the structure in which it is initially positioned underwent a fission into two structures. The trapping period of these structures is around 2. Note that although these particles are both trapped, their orbits are much less regular than the trapped particles that were observed in the decaying turbulence. That these are the least regular trajectories observed is consistent with the fact that run B had the broadest frequency spectrum for the strongest mode.

The trajectories of C1 and C2 are shown in Fig. 14(c). The frequency spectrum in run C was much less broad ($\Delta\omega/\omega\approx 20\%$), and indeed, the trajectories look much more like the decaying turbulence trajectories, though somewhat less regular.

Finally, Fig. 14(d) shows the trajectories of D1 and D2. These two particles were initially placed close together, and both were trapped within the same structure. Their trajectories illustrate the nonchaotic nature of the trapped structure in that the two trajectories do not diverge exponentially from each other, as they would if they were in an untrapped region of the turbulence. This fundamental qualitative difference in behavior of trapped and untrapped particles is the cause for concern with renormalized perturbation theories. These theories generally make some sort of random phase approximation or maximal randomness approximation, which is not consistent with the behavior of the fluid observed inside of a trapped structure.

In each of the four runs we found trapped structures that lasted for the full length of the run (12.5 drift periods). The evolution of these structures is much different from the purely damped case, however. The structures change shape, and wander about in the x direction during the course of the run. Also, the trapped particle orbits are much less regular than in the cases of an isolated monopole or decaying turbulence, with the level of irregularity being correlated with the width of the frequency spectrum. One is tempted to say that the structure lifetime should be given by $\tau_s\approx 2\pi/\Delta\omega_k$. For the strongest modes in runs A–D $\tau_s\approx 26$–150. Unfortunately, our simulations did not run this long, since doing so would have been impractical (integrating the oscillatory particle trajectories requires a much smaller time step than integrating the fields alone). Observation of movies of ρ contours shows that the structures can be very robust, however, surviving very strong interactions with other vortices. We have, in fact, observed particles trapped for more than 20 trapping times for a run very similar to run D. In these runs, where the electric field is quite strong, the width of the frequency spectrum seems to be more related to the time scale over which the vortices are perturbed than to the vortex lifetime.

VI. CONCLUSIONS

Our research has shown that there is a strong tendency for trapped structures to form in decaying Hasegawa–Mima turbulence and that these structures may persist in driven-damped turbulence.

For the Hasegawa–Mima simulations, the following picture of the turbulent decay emerges: First, the system quickly relaxes from the initial random-phase state to a much more coherent state. During this relaxation there is a rapid change in the shape of the energy spectrum, with the average k vector decreasing rapidly. When the average k vector gets below $k\approx 1$, the relaxation slows dramatically. A quasisteady state is achieved, with smaller vortices slowly merging to form larger vortices, moving the average k vector slowly (very slowly) toward $k_{\min}$.

In this quasisteady regime, the high-k part of the spectrum is basically shape preserving, with a slope of around k^{-4}–k^{-6}. Although this shape, as well as the other observations, does not seem to be tremendously sensitive to the magnitude of the viscosity, our runs had a fairly low viscous Reynolds number, and so it is not clear proof that the k^{-3} spectrum is incorrect.

For $k\ll 1$ the spectrum does not really attain a steady shape. Energy continues to build up at the lowest wave numbers while the rest of the spectrum slowly dies away. This may be an indication of the low-k spectrum trying to move toward the equilibrium state. However, it appears to be happening at a relatively slow rate.

We also observed that the fluctuations in the ρ field were qualitatively similar to an identical run using a model with no density gradient. However, there were fewer trapped structures in the finite density gradient case, and

the vorticity field for these two cases was quite different. Our interpretation of this is that the tendency of trapped structures to evolve is very similar to the fluid dynamics case. However, the constraints placed on the system by the existence of the density gradient modify the manner in which these vortices can interact, giving them a new means by which to become untrapped, and modifying the way in which energy is dissipated.

Finally, the frequency spectrum, although not quantitatively measurable in this decaying regime, appeared to be fairly narrow. This is a very important observation because it is strongly at odds with the experimental facts. It is also somewhat at odds with the intuitive feeling that a strongly nonlinear system, which we certainly have here, will always be characterized by a broad frequency spectrum.

The addition of the nonadiabatic electron model developed in Sec. II has several important effects on the evolution of the turbulence. The nonadiabatic electrons contribute in an important way to the saturation of the turbulence. This saturated state is characterized by a broader frequency spectrum than in the case of decaying turbulence. In spite of this broader spectrum, however, long-lived trapped structures still evolve in the flow.

The most significant effect of the nonadiabatic electrons seems to be the strong dissipation they provide for high-k modes and modes along the k_x axis. This dissipation mechanism is quite complex and is responsible for the somewhat nonintuitive result that increasing the strength of the nonadiabatic electron term, which is usually thought of as a source term, results in a decrease in the saturation energy. This is a good example of how our intuition, based on linear theory, can lead us far astray when trying to understand a strongly nonlinear problem.

Although the frequency spectra were found to be quite broad at high k, in the energy containing region, $k < 1$, the spectral linewidths were only narrow to moderately broad. We showed that this result is an inherent shortcoming of the model; a stationary state cannot be maintained with all the modes having $\Delta\omega \geqslant \omega$.

A few additional trends were noticed: The saturation levels depend only weakly on the magnitude of the hyperviscosity coefficient, ν_4. This is a comforting result, since the viscous models for this problem are really quite unjustifiable. Most of the saturation values depended strongly on the maximum linear growth rate, $\gamma^L_{\max}$, except for the rms electric field. This quantity was found to depend only on the nonadiabatic cutoff, k_n. Thus, for a given k_n, the system seems to have a critical electric field that is very important in the saturation process.

In all cases, the saturated electric field was sufficiently high for trapping to occur, and in spite of the broadened frequency spectrum, coherent trapped structures were observed in many runs. This is counter to speculation by some authors that driving the system in the energy-containing region would destroy any coherent structures that might otherwise develop.[14,31]

Although trapping occurred in all of the runs, it was not a dominant effect in all cases. As the electric field increased, so did the predominance of trapped structures. We observed that the flow inside the trapped structure was very nonchaotic, in spite of the fact that the overall flow was quite turbulent. We also observed that, as the width of the frequency spectrum increased, the motion and shape of the trapped structure became more erratic. However, the relative motion of two particles trapped within the same structure was still regular. This regularity within chaos appears to be at odds with the assumptions made by many renormalized turbulence theories. We note that the "hole" theory which Dupree has applied to one-dimensional Vlasov turbulence[32–35] does attempt to deal with similar long-lived structures in a different context. Terry *et al.*[36] have applied this theory to electron drift waves, but they only considered the case of isolated electron drift holes moving faster than the diamagnetic drift speed (and thus not interacting with each other or with the waves). Whether these theories can be successfully applied to the problem at hand remains to be seen.

The fact that the nonadiabatic electron model plays such an important role in the qualitative nature of the turbulence shows that close attention should be paid to how such effects are included. In some ways this makes our model inconsistent, since several effects were neglected that might be just as important as the nonadiabatic electron terms that we have tried to simulate.

Simulation of a real system was not the goal of this research, however; rather, we were interested in studying trapped structures in a driven-damped system with the most realistic nonadiabatic electron model that we could derive in two dimensions. Our model was perfectly suitable for this task. Indeed, it would be interesting to compare renormalized turbulence theories to this model, especially for runs such as run D, which exhibited very strong trapping along with a fairly broad frequency spectrum. We leave this problem to future work.

ACKNOWLEDGMENTS

We wish to thank Professor P. Diamond, Professor W. Horton, and Professor K. Molvig, and Dr. A. Koniges, for many useful discussions.

This work was performed under the auspices of the U.S. Department of Energy—at the Massachusetts Institute of Technology, under the Magnetic Fusion Energy Science Fellowship Program, which is administered for the Department of Energy by Oak Ridge Associated Universities; and at Lawrence Livermore National Laboratory under Contract No. W-7405-ENG-48.

[1] A. Hasegawa and K. Mima, Phys. Rev. Lett. **39**, 205 (1977).
[2] A. Hasegawa and K. Mima, Phys. Fluids **21**, 87 (1978).
[3] D. Fyfe and D. Montgomery, Phys. Fluids **22**, 246 (1979).
[4] R. E. Waltz, Phys. Fluids **26**, 169 (1983).
[5] P. Terry and W. Horton, Phys. Fluids **25**, 491 (1982).
[6] P. W. Terry and W. Horton, Phys. Fluids **26**, 106 (1983).
[7] W. Horton, Phys. Fluids **29**, 1491 (1986).
[8] W. Horton, Phys. Fluids B **1**, 524 (1989).
[9] B. B. Kadomtsev, *Plasma Turbulence* (Academic, London, 1965).
[10] T. H. Dupree, Phys. Fluids **9**, 1773 (1966).
[11] R. H. Kraichnan, J. Fluid Mech. **5**, 497 (1959).
[12] T. H. Dupree, Phys. Fluids **15**, 334 (1972).

[13]V. I. Petviashvili and O. A. Pokhotelov, Sov. J. Plasma Phys. **12**, 651 (1986).
[14]J. C. McWilliams, J. Fluid Mech. **146**, 21 (1984).
[15]R. H. Kraichnan and D. Montgomery, Rep. Prog. Phys. **43**, 547 (1980).
[16]D. G. Fox and S. A. Orszag, Phys. Fluids **16**, 169 (1973).
[17]J. D. Meiss and W. Horton, Phys. Fluids **26**, 990 (1983).
[18]P. C. Liewer, Nucl. Fusion **25**, 543 (1985).
[19]S. A. Orszag, Stud. Appl. Math. **L**, 293 (1971).
[20]S. A. Orszag, J. Fluid Mech. **49**, 75 (1971).
[21]D. Gottlieb and S. A. Orszag, *Numerical Analysis of Spectral Methods: Theory and Application* (SIAM, Philadelphia, PA, 1977).
[22]D. Gottlieb, M. Y. Hussaini, and S. A. Orszag, in *Spectral Methods for Partial Differential Equations*, edited by R. G. Voigt, D. Gottlieb, and M. Y. Hussaini (SIAM, Philadelphia, PA, 1984), pp. 1–54.
[23]S. A. Orszag and G. S. Patterson, Jr., Phys. Rev. Lett. **28**, 76 (1972).
[24]D. G. Fox and S. A. Orszag, J. Comput. Phys. **11**, 612 (1973).
[25]J. W. Cooley and J. W. Tukey, Math. Comput. **19**, 297 (1965).
[26]J. A. Crotinger, Ph.D. thesis, Massachusetts Institute of Technology, 1989.
[27]V. D. Larichev and G. M. Reznik, Oceanol. **15**, 113 (1975).
[28]G. R. Flierl, V. D. Larichev, J. C. McWilliams, and G. M. Reznik, Dyna. Atmos. Oceans **5**, 1 (1980).
[29]J. Nycander, Phys. Fluids A **4**, 467 (1991).
[30]This argument is not without criticism. We have observed simulations of this and other models in which a single mode would come to dominate the evolution and basically grow without bound at the linear growth rate.
[31]A. Hasegawa, Adv. Phys. **34**, 1 (1985).
[32]T. H. Dupree, Phys. Fluids **25**, 277 (1982).
[33]T. H. Dupree, Phys. Fluids **26**, 2460 (1983).
[34]T. H. Dupree, Phys. Fluids **29**, 1820 (1986).
[35]T. H. Dupree, Phys. Fluids **29**, 1813 (1986).
[36]P. W. Terry, P. H. Diamond, and T. S. Hahm, Phys. Fluids B **2**, 2048 (1990).